Fluid Flow Investigations within a 37 Element CANDU Fuel Bundle Supported by Magnetic Resonance Velocimetry and Computational Fluid Dynamics

M.H.A. Piro[a,*], F. Wassermann[b], S. Grundmann[b,c], B. Tensuda[d], S.J. Kim[e], M. Christon[f], M. Berndt[g], M. Nishimura[a,h] and C. Tropea[b]

[a] *Fuel and Fuel Channel Safety Branch, Canadian Nuclear Laboratories, Chalk River, ON, Canada*
[b] *Department of Fluid Mechanics and Aerodynamics, Technische Universität Darmstadt, Darmstadt, Germany*
[c] *Institute of Fluid Mechanics, University of Rostock, Rostock, Germany*
[d] *University of Toronto Institute for Aerospace Sciences, University of Toronto, Toronto, ON, Canada*
[e] *Mechanical and Thermal Engineering, Los Alamos National Laboratory, Los Alamos, NM, USA*
[f] *Computational Sciences International, Los Alamos, NM, USA*
[g] *Computer, Computational and Statistical Sciences, Los Alamos National Laboratory, Los Alamos, NM, USA*
[h] *Computer Science Department, University of Waterloo, Waterloo, ON, Canada*

* Corresponding author: +1 613 584 8811 x 42530; markus.piro@cnl.ca.

Abstract

The current work presents experimental and computational investigations of fluid flow through a 37 element CANDU nuclear fuel bundle. Experiments based on Magnetic Resonance Velocimetry (MRV) permit three-dimensional, three-component fluid velocity measurements to be made within the bundle with sub-millimeter resolution that are non-intrusive, do not require tracer particles or optical access of the flow field. Computational fluid dynamic (CFD) simulations of the foregoing experiments were performed with the HYDRA-TH code using implicit large eddy simulation, which were in very good agreement with experimental measurements of the fluid velocity. Greater understanding has been gained in the evolution of geometry-induced inter-subchannel mixing, the local effects of obstructed debris on the local flow field, and various turbulent effects, such as recirculation, swirl and separation. These capabilities are not available with conventional experimental techniques or thermal-hydraulic codes. The overall goal of this work is to continue developing experimental and computational capabilities for further investigations that reliably support nuclear reactor performance and safety.

Keywords

Nuclear; CANDU; magnetic resonance velocimetry; computational fluid dynamics; large eddy simulation.

1   Introduction

Understanding fluid flow through a CANDU nuclear fuel channel is important from both performance and safety points of view under normal operating and upset[1] conditions since the coolant provides a heat sink for the fuel. Typically, thermal-hydraulic predictions of coolant circuits and fuel channels in a CANDU reactor are performed by the system level code CATHENA [1] or the subchannel level code ASSERT-PV [2], which have been developed at the Canadian Nuclear Laboratories (CNL; formerly Atomic Energy of Canada Limited). More recently, CNL has been developing its Computational Fluid Dynamics (CFD) capabilities [3,4] to complement its system level and subchannel level code suite to capture fluid behaviour with a much higher degree of resolution than what was previously possible with conventional thermalhydraulic codes. While great progress has

---

[1] Upset conditions include, but are not limited to, partial loss of power, coolant flow or coolant system pressure.

been made in contemporary approaches based on CFD, any analyses that support nuclear reactor safety must ultimately be validated by carefully designed and executed experiments.

Conventional experimental and computational investigations of fluid flow through a fuel channel have been limited by physical or computational constraints that result in overly conservative assumptions and an underlying uncertainty about the flow field. Established fluid flow instruments – such as pitot tubes, Laser Doppler Velocimetry (LDV) or Particle Image Velocimetry (PIV) – are ineffective at reliably measuring fluid velocity within a CANDU fuel channel due to their intrusive nature or due to lack of optical visibility of the fluid regime within the fuel channel. While progress has been made using LDV and PIV for Light Water Reactor (LWR) applications using Refractive Index Matching (RIM), the same techniques cannot be effectively applied to CANDU fuel channels for geometric reasons. First, LWR fuel rods are very long and predominantly cylindrical, whereas CANDU fuel rods are relatively short and have appendages, which play an important role that must be considered. Manufacturing an optically transparent bundle replica with appendages is problematic. Second, LWR fuel assemblies are rectangular with rods arranged on a structured grid, which permits optical visibility of the interior of the assembly with careful control of optics, whereas CANDU fuel bundles are cylindrical. Therefore, lasers must traverse multiple solid/liquid interfaces to measure fluid velocity in the interior of the bundle, which can result in significant error due to refraction despite the best efforts in employing RIM techniques.

Although computational predictions of thermal-hydraulic behaviour that are made with conventional codes are generally in good agreement with available experimental measurements, they typically rely heavily on empirically tuned correlations that are not universal in nature and are also unable to capture local effects with high spatial resolution. For example, one could not reliably extend such a framework from subchannel flow through a fuel bundle in a normal pressure tube to a deformed pressure tube, which may experience considerable diametral creep towards end of life resulting in flow bypass effects.

Many of the aforementioned concerns have been eliminated by recent advances in experimental and computational methodologies. Magnetic Resonance Velocimetry (MRV) permits all three components of the time-averaged velocity vector field to be measured in three dimensions without requiring optical access to the measurement volume, injection of tracer particles or physically intruding the flow field. The MRV technique is based on Magnetic Resonance Imaging (MRI), which has demonstrated many practical applications for medical [5,6] and engineering flows [7,8]. Similarly, recent advancements in CFD, compounded by the availability of affordable high performance computing resources, facilitate the detailed simulation of complex fluid flow problems with sophisticated turbulence models, in particular models capable of capturing the anisotropy inherent in such flows.

In the current work, MRV measurements of light water flowing through a CANDU fuel channel replica have been performed, which provide time-averaged, three-dimensional, three-component velocity measurements within the fuel bundle. Moreover, the CFD code HYDRA-TH [9] was used to predict time-dependent fluid dynamic behaviour within the bundle. An Implicit Large Eddy Simulation (I-LES) model was used to capture the turbulent flow behaviour, which does not rely on the isotropic eddy-viscosity assumption while also resolving large eddies directly. The flow conditions that are analyzed in this work are not representative of in-reactor conditions (specifically, lower temperature, pressure and mass flow rate). However, the intent of the work is to further develop capabilities for understanding and predicting fluid flow through a fuel channel with a much higher degree of resolution than what has been previously possible. Together, these experimental and computational tools are intended to provide confidence in the analysis techniques described herein, which are envisioned to investigate more realistic in-reactor conditions in future work to support performance and safety analyses.

2   Experimental Considerations

2.1   Experimental Setup

A typical CANDU fuel bundle, which is illustrated in Figure 1a, contains 37 fuel elements[2] that are concentrically arranged and mounted on two end plates.   The total length of a bundle is approximately 500 mm and the diameter is about 100 mm. Spacer pads are appended to the fuel elements to prevent adjacent elements from contacting one another and bearing pads are appended on the outer elements to provide spacing with the pressure tube wall. Depending on the particular plant, 12 or 13 bundles are horizontally arranged in a string within a pressure tube. The configuration of a bundle sitting within a pressure tube, which also resides within a calandria tube, is shown in Figure 1b. Pressurized heavy water flows through each fuel channel with a mass flow rate of ~24 kg/s and a Reynolds number of about 3 million at the inlet of a fuel channel, which is calculated from the inner diameter of the pressure tube.
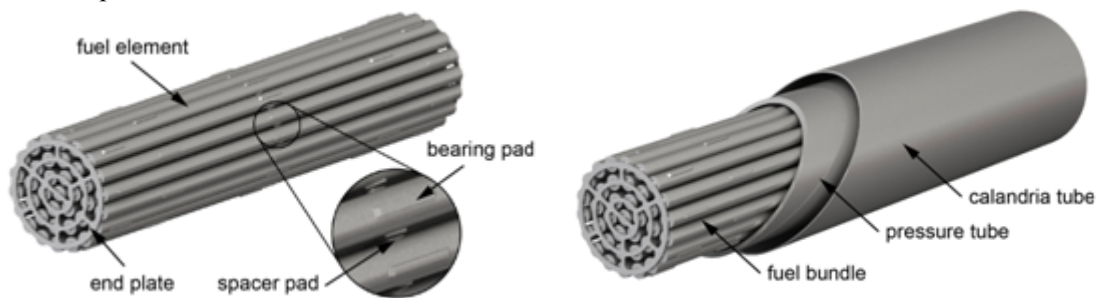

Figure 1. a) Isometric view of a 37 element CANDU fuel bundle, and b) the configuration of a CANDU fuel channel including the fuel bundle, pressure tube and calandria tube [4].

A replica of the CANDU fuel bundle shown in Figure 1 above was manufactured using direct polyamide laser sintering and is shown in Figure 2. The bundle was manufactured in two halves due to size limitations of the laser-sintering machine, and the two parts were mated together with a tongue and groove fixture with adhesive. During the manufacturing process, the sintered parts densified during the cool-down phase. The final fuel element diameter was measured with a vernier caliper to be 12.9 mm, which is very close to the actual geometry of 13.08 mm (i.e., ≈1% difference) [10]. The current bundle is surrounded by a tube with an Inner Diameter (ID) of 102 mm and an Outer Diameter (OD) of 110 mm, which was made of acrylic glass. Due to fabrication tolerances, the ID was measured to be 102.5 mm with a vernier caliper, which is less than 1% from the actual geometry [10]. The relative difference in the cross-sectional area of the fluid region between the MRV experiment and commercial specification is ≈0.3%, which is inconsequential.

The entire flow model including the fuel bundle is depicted in Figure 2 below. The fuel bundle was axially fixed with a pin attached to a thin plate located inside the downstream end nozzle. Immediately upstream from the fuel bundle, a nozzle accelerates the fluid from the settling chamber with an ID of 150 mm. Both the settling chamber and the end nozzle contain de-aeration holes, which permit air bubbles to escape but not water. Upstream from the settling chamber, a wide-angle diffuser with multiple diffuser grids preconditions the flow. The intent of preconditioning is to generate a uniform velocity profile immediately upstream from the bundle, which is favourable for simulation purposes. A detailed discussion of the manufacturing of the pre-conditioner is given by Wassermann [11].

---

[2] A 28-element bundle design is also used in some commercial CANDU power generating stations.
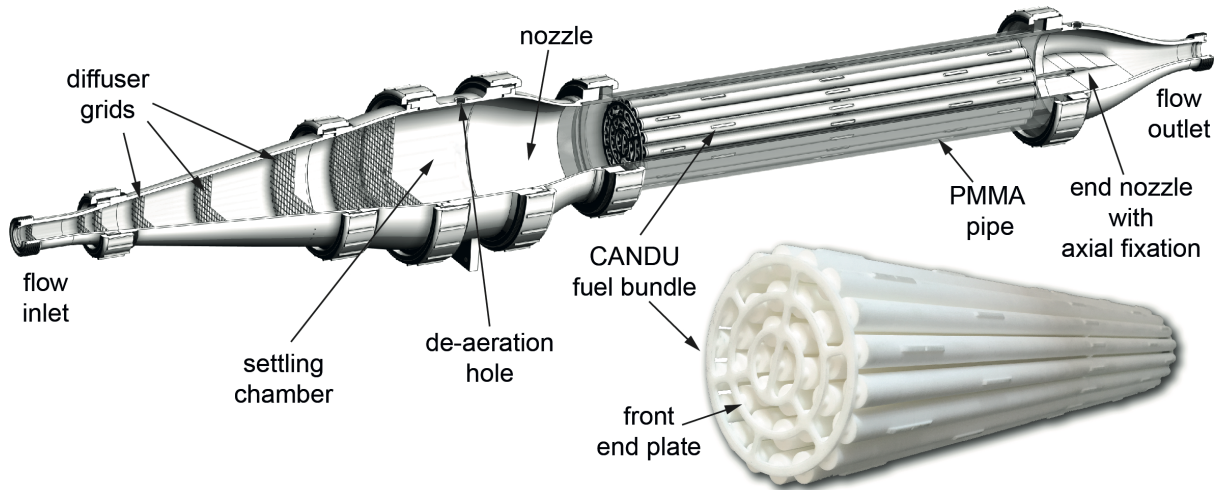
Figure 2. A schematic is shown of the flow apparatus. A diffuser adapts the inlet of the flow rig to the region containing the fuel bundle with multiple intermittent diffusers. The nozzle downstream from the bundle converges to the return line. A photograph shows the laser sintered polyamide bundle used in the MRV measurements. The manufactured bundle is a geometrically accurate representation of a CANDU fuel bundle. Graphic adapted from Wassermann [11].

The operating fluid was deionised light water with 1 g/L copper sulfate salt as a contrast agent, which was added to the water to enhance signal quality without affecting fluid transport. The flow loop was prepared with a flow supply system and was adjusted to 60 L/min [11]. The fluid temperature was maintained constant at 21 °C using an immersion cooler (Julabo FT402, Seelbach, Germany) inserted into the 100 L fluid reservoir. The resulting Reynolds number was approximately 12,500, as calculated with the ID of the pressure tube.

The Reynolds number in this experiment was much lower than what is typically experienced in-reactor. The main limitation in reproducing these conditions ultimately rests on materials that are compatible with an MRI. Specifically, non-metals must be used, which is why the bundle replica and the preconditioner were manufactured using polyamide powder via additive manufacturing. Furthermore, the very high flow rate of ~24 kg/s of water flowing through a multi-million euro MRI poses a legitimate risk of water leakage with subsequent damage to electronics, which could potentially be resolved given appropriate engineering design changes. Nevertheless, the intent of this work is to further progress capabilities of investigating fluid flow inside a fuel bundle to high spatial resolution with the understanding that it is not representative of normal operating conditions in-reactor.

2.2 Measurement Parameters

The measurement principle of MRV is based on the magnetic interaction of the hydrogen nucleus with external magnetic and electromagnetic fields. This also implies that no optical access is necessary. The measurement fluid just needs magnetic and electromagnetic access. In the presence of a strong magnetic field, the hydrogen nucleus starts to precess with a unique frequency, called the Larmor frequency, which depends on the magnetic field strength. Such precessing hydrogen nuclei can be excited with electromagnetic pulses that are also oscillating at the Larmor frequency and emit electromagnetic signals (Magnetic Resonance (MR) signal) that can be received by sensitive coils. The Larmor frequency of each macroscopic ensemble of hydrogen nuclei (called Voxel, typically a cube with ~1 mm edge length) can be altered in space and time by altering the magnetic field using magnetic field gradients. This process is known as spatial encoding. Thus, the spatially encoded MR signal can be received and the information in each voxel can be reallocated to its spatial position. Additionally, by applying bipolar velocity-encoding gradients, the velocity information can be detected in each voxel. This enables the measurement of three-dimensional, three-component (3D3C) velocity fields.

4

For MRV measurements, the Siemens TIM Prisma system (Erlangen, Germany) operating with a 3 Tesla main magnetic field strength was utilized. The chosen MR settings are summarized in Table 1. Velocity data were acquired in five separate Field-Of-Views (FOVs) with consistent MR settings. Each FOV was acquired with a 3D gradient echo Fast Low Angle Shot (FLASH) sequence where the Frequency Encoding (FE) and Phase Encoding (PE) axes were aligned with the Cartesian Z- and X-directions, respectively. Despite the fact that the utilized MR machine is designed for high performance measurements, field distortions can arise from inhomogeneities in the magnetic system when using large flow models exceeding the dimensions of the magnetic iso-centre. Hence, the entire geometry was partitioned into five sections (~100 mm each) in the axial (Z) direction for measurement purposes and then merged during post-processing. For each scan, the table was moved 100 mm by the scanner controls with an uncertainty of approximately 1 mm; each time shifting the FOV. The channels of the applied receiver coils were toggled on and off according to the table position. For each FOV, an additional scan without flow and equal MR parameters was acquired to enable a background phase correction utilizing a 3D fit routine provided by Testud and Zaitsev [12].

A quantitative measure of data quality is the Signal-to-Noise Ratio (SNR). For the presented data, a magnitude threshold of 60 was chosen with the help of a statistical histogram plot to separate the noise from the signal [13]. Additionally, the magnitude threshold was used for masking the material structure. The choice of the magnitude threshold can influence the appearance of the data significantly, especially in regions where high signal loss is present. The SNR can be calculated with the signal background method [13]. The velocity error due to phase noise is proportional to the reciprocal of the SNR and can be calculated according to methods described by Bernstein [5]. Both are listed in Table 1. By this procedure, an overall SNR of the dataset is determined, which allows one to quantify a single velocity uncertainty for the whole dataset. More advanced methods for quantifying location dependent velocity uncertainty are currently under development.

Table 1. Imaging parameters and MR settings of the MRV acquisitions [11].

MR Parameter	Value
Repetition time/Echo time [ms]	36.8/5.2
Flip Angle [°]	15
Pixel bandwidth [Hz/pixel]	445
Spatial Resolution [mm]	0.8 isotropic
FExPE lines (Z- x X-direction)	256x144
Slices (Y-direction)	144
Channels	14
Total acquisition time [min]	15
Averages	1 (2 for FOV 1)
Venc [m/s]	0.5
SNR	13.1
Velocity error [m/s]	0.03

2.3   Magnetic Resonance Data Consistency

The data set has been composed of five different acquisitions and will heretofore be referred to as FOV1 to FOV5. Data consistency in transitioning from one FOV to the neighbouring FOV must be verified. For this reason, the cross-sectional averages along the Z-direction of the velocity components U_x, U_y and U_z (streamwise component) were derived. Additionally, the flow rate was integrated over all cross-sections to ensure continuity is satisfied. All curves are shown in Figure 3.
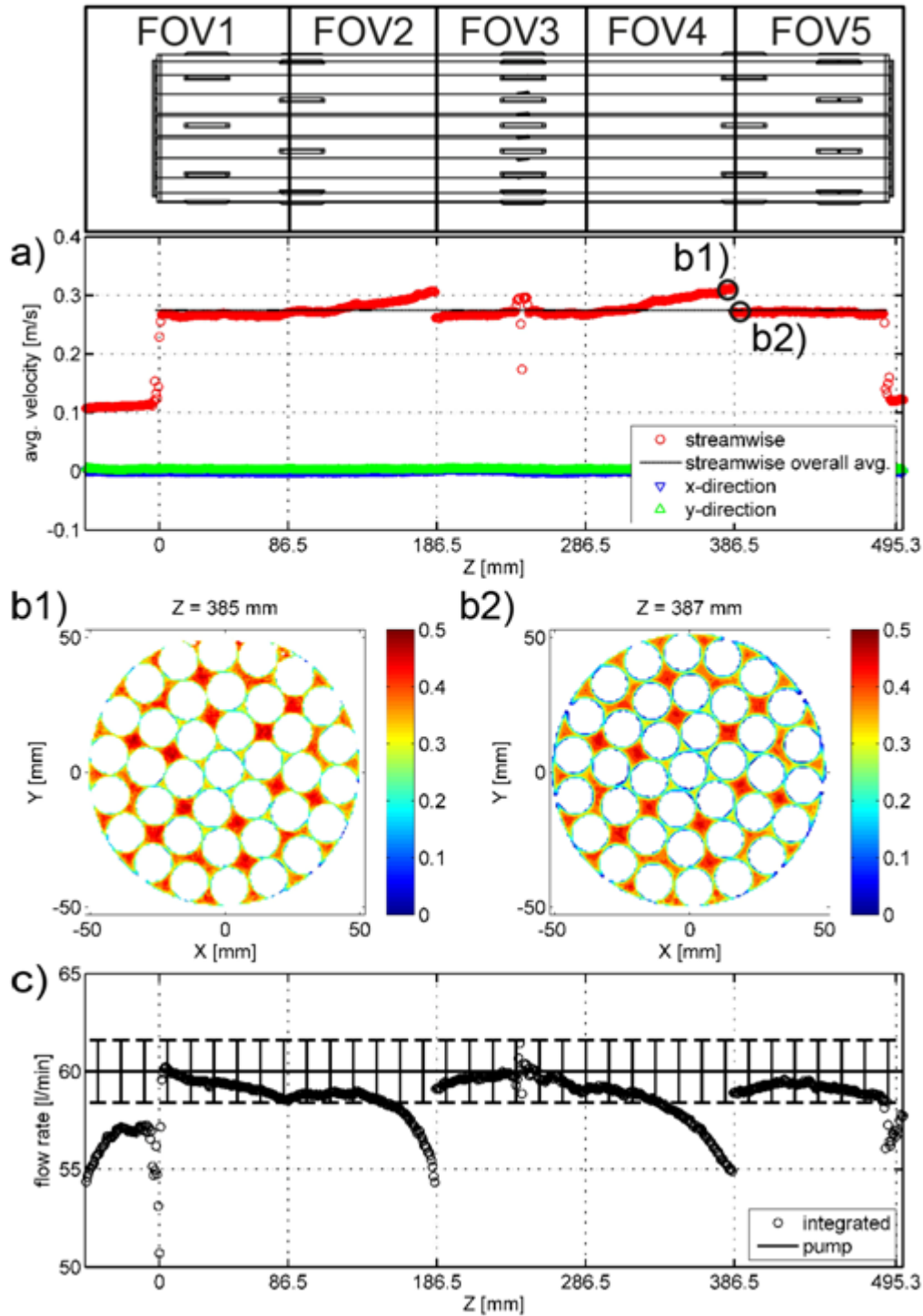
Figure 3. a) Cross-sectional integrated measured velocity components in X-, Y- and Z-directions; b1) and b2) show contour plots of the streamwise velocity at two axial locations (marked with O in (a)) in neighbouring fields of view; c) volumetric flow rates along the axial direction are calculated by integrating the axial velocity component from MRV data. The volumetric flow rate provided by the pump is provided with uncertainty bars to provide an indication of the overall measurement error. Graphic adapted from Wassermann [11].

In Figure 3a, the cross-sectional averages of the cross-stream components (i.e., U_x and U_y) are considered. Both velocity components are near zero, which verifies that the inflow was sufficiently pre-conditioned and that the applied background phase correction was done properly. Secondly, the cross-sectional averaged streamwise velocity component (i.e., U_z) is shown in Figure 3a and compared to the overall average (dashed line). Good agreement is found over a wide range across the Z-coordinate.

The U_z average velocity increases towards the ends of FOV2 and FOV4. Figures 3 (b1) and (b2) show contour plots of the streamwise velocity component at Z = 385 mm (i.e., downstream position of FOV4) and Z = 387 mm (i.e., upstream position of FOV5). Upon closer examination, the fuel elements shown in Figure 3 (b1) appear larger in diameter compared to Figure 3 (b2), which is physically not possible as each bundle half was manufactured in one process. The gaps between neighbouring elements appear smaller for Figure 3 (b1) than for Figure 3 (b2). The blue regions adjacent to the fuel elements (i.e., velocity boundary layer) are absent in Figure 3 (b1). The reason for that was an inappropriate selection of the receiver coil channels for FOV2 and FOV4 that lead to a reduced signal towards the ends of both FOVs. Hence, the signal in the regions around the fuel elements, which already suffers from partial volume artifacts (e.g., signal drop out in voxels that are partially filled with fluid and solid material of the flow model), and the signal in the upper periphery of the bundle decreases below the magnitude threshold of 60. This was recognized after the measurements were completed and during post-processing. This explains the increase of the cross-sectional average of U_z in Figure 3a for FOV2 and FOV4. Nevertheless, the velocity values per voxel are consistent for both contour plots. Hence, issues are only present for the signal magnitude but not for the signal phase, which means that the cross-stream velocity components are not affected. The cross-sectional averaged or integrated values are affected as they require a complete representation of all voxels. Hence, these areas are marked in the subsequent plots.

Figure 3c compares the integrated flow rate to the bulk flow rate provided by the flow supply system (denoted with pump). Both curves show good agreement and the integrated flow rate lies within the error bars of the ultrasound flow rate sensor utilized in the flow supply system. The flow rate curve in FOV2 and FOV4 is affected according to the cross-sectional integrated streamwise velocity component discussed above. Measurement error is relatively high in the middle section of FOV3 and through the front and rear end plates, as evidenced by the departure from continuity in Figure 3. This error is due to insufficient spatial resolution and errors due to flow acceleration. For Z < 0 mm, the flow rate is noticeably below 60 L/min. The error is relatively high in this region because it is outside the magnetic iso-centre; hence, distortions can occur that artificially reduce the effective cross-sectional area [5].

3   Computational Considerations

The CFD code HYDRA-TH was used in this work to simulate the experiments described in section 2. HYDRA-TH is a subset of the Hydra Toolkit and it provides a general-purpose capability for simulating incompressible and low-Mach number flows. HYDRA-TH has been used by Los Alamos National Laboratory for the Consortium for Advanced Simulation of Light water reactors (CASL) to address a number of single phase applications for a wide range of nuclear industry thermal-hydraulic applications, such as grid-to-rod fretting [14]. The Hydra Toolkit is a massively parallel multi-physics framework that is written in C++ and provides a rich suite of lightweight high performance components that permit rapid application development, supports multiple discretization techniques, provides I/O interfaces to permit reading and writing multiple file formats for meshes, plot data, time-history, surface and restart output.

For this problem, HYDRA-TH solved the time-dependent partial differential equations representing continuity and momentum under isothermal conditions. The continuity equation for an incompressible isothermal fluid is given by

$$\frac{\partial \bar{u}_i}{\partial x_i} = 0 \qquad (1)$$

where u_i is the instantaneous velocity component in the direction of x_i and the over-bar indicates a filtered quantity. The time dependent momentum equation in an inertial reference frame is given by

$$\frac{\partial \rho \bar{u}_i}{\partial t} + \frac{\partial}{\partial x_j}\left(\rho \bar{u}_i \ \bar{u}_j \ \right) = -\frac{\partial \bar{p}}{\partial x_i} + \frac{\partial}{\partial x_j}\mu\left(\frac{\partial \bar{u}_i}{\partial x_j} + \frac{\partial \bar{u}_j}{\partial x_i}\right) - \frac{\partial \tau_{ij}}{\partial x_j} \tag{2}$$

Here, fluid density is denoted by ρ, time by t, pressure by p, the dynamic viscosity by μ and the stress tensor by τ. The stress tensor is model dependent, which will be given more careful consideration in the following section.

3.1   Turbulence Modelling

The fluid transport for this problem is bounded by numerous walls, and is affected by the overall complexity of the geometry. For instance, the front and rear end plates induce rotation, the skewed spacer pads induce swirl and the combination of various effects lead to inter-subchannel mixing. Needless to say, accounting for turbulent anisotropy is important, as is the viscous near-wall region.

Several previously published articles that have investigated fluid flow through a CANDU fuel bundle have independently come to the same conclusion that turbulence models based on the Reynolds Averaged Navier-Stokes (RANS) equations are inadequate for this particular flow problem, which have been supported by experimental measurements [4,15,16]. Furthermore, RANS models under-predict inter-subchannel mixing in a fuel bundle due to its inability to capture turbulent anisotropy or quasi-periodic flow (for steady state cases) [17]. In this study, an Implicit-LES (I-LES) model [18] was utilized to evaluate the time-dependent flow characteristics in the wall-bounded flow through a CANDU fuel bundle.

There are many variants of LES that have been developed, and the characteristics and advantages of these methods relative to RANS models are relatively well known. The many aspects of LES, and in particular I-LES, are beyond the scope of this paper. Here, only the relevant aspects of I-LES are outlined. I-LES, in contrast to conventional explicit subgrid-scale (SGS) models, hinges on the concept associated with the numerical regularization of the resolved-scale numerics due to the effects of SGS fluid dynamical effects. Numerical methods that "build-in" this regularization may be found in stabilized finite element methods and some monotonicity-preserving finite volume methods [18]. In addition, a detailed presentation of modified equation analysis and assessment of high-resolution (monotonicity-preserving) algorithms is described by Grinstein *et al* [18]. A spectral analysis of the interplay between advective phase (and group) speed and dissipation for signals ranging from the integral to the grid Nyquist limit is described by Christon *et al* [19,20]. The modified equation analysis is important in defining the form of implicit SGS terms, HYDRA-TH also considers the spectral analysis that is critical in designing I-LES methods that accurately represent the grid-resolved eddies. The details of the non-linear, monotonicity-preserving advection scheme, and the associated phase speed and dissipation may be found in the HYDRA-TH Theory Manual [9].

In contrast to an explicit SGS approach, the I-LES formulation used in HYDRA-TH does not rely on filtering concepts with a $2\Delta x$ cut-off (i.e., "energy drain"). Instead, a balance between phase speed and dissipation is constructed in a non-linear and monotonicity preserving procedure that respects the energy cascade throughout the discrete spectrum. The application of I-LES to a turbulent flow problem is not unlike the practices used for explicit SGS models. In HYDRA-TH, wall-functions are not used for I-LES, requiring a mesh resolution down to a y^+ ~1 for near wall cells.

An automatic time-step controller is used with a fixed maximum Courant-Friedrichs-Levy (CFL) condition in order to capture the eddy-turnover time scale associated with eddies in the regions between the rods of the bundle. Preliminary computations were carried out to assess the time-scale when a statistically stationary flow is established using the integrated kinetic energy of the flow domain as a metric to establish the presence of a clear mean flow and associated turbulent fluctuations. This time-scale determined the starting point for the collection of turbulent statistics for

the flow problem with refined meshes. HYDRA-TH provides a rich set of tools for instrumenting a flow simulation and collecting turbulent statistics that include means, variances, RMS values, turbulent kinetic energy and Reynolds stresses.

3.2   Geometry and Mesh Generation

For the sake of consistency, the geometry of the CANDU fuel bundle used in the CFD simulations was made using the same CAD model that was used to manufacture the polyamide bundle shown in Figure 2. The simulated geometry is shown in Figure 4, which also identifies the inlet, outlet, channel wall and the 37-element fuel bundle. This model is a correct geometric representation of a CANDU 37 element fuel bundle used in the Bruce Nuclear Generating Station in Canada. The computational geometry also included the pressure tube with a 0.89 mm radial gap, 50 mm upstream fluid region and 150 mm downstream fluid region.

In the experiment, a large diffuser adapts the flow supply system at the inlet of the test rig containing the fuel bundle with a nozzle at the outlet. Again, the pre-conditioning system shown in Figure 4 used in the experiments was designed to produce a uniform velocity profile at the inlet of the test rig, which eliminates the need of including it in the computational geometry. Figure 5 shows the measured axial velocity near the inlet is fairly homogeneous. While a uniform velocity profile upstream from a bundle is not representative of in-reactor conditions, it was intended to facilitate comparison between measurements and predictions for this analysis.
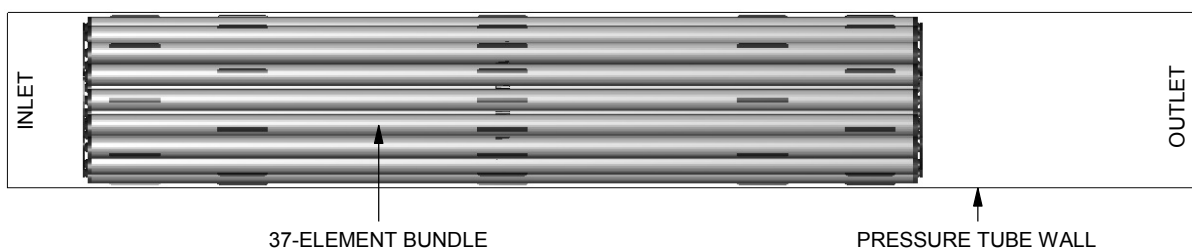

Figure 4. A schematic of the simulated geometry with the inlet, outlet, channel wall and 37-element bundle identified.
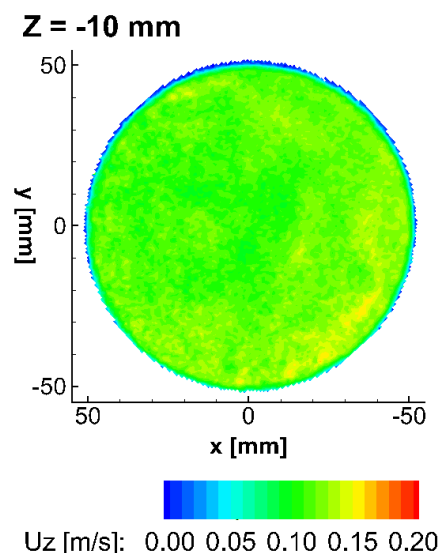

Figure 5. Measured axial velocity contour plot upstream of the 37-element fuel bundle, at the position z = -10mm. The contour demonstrates a very uniform flow velocity, with slightly higher velocities towards the bottom right region of the channel.

The geometry of the bundle was constructed with SOLIDWORKS [21], which was then meshed with HEXPRESS/HYBRID [22]. HEXPRESS/HYBRID was chosen for its ability to automatically generate high quality hex-dominant meshes directly from CAD geometries, which proved to be very effective for such a highly complex geometry. Table 2 summarizes the mesh size and quality statistics, which includes the distribution of mesh cell types. Observe that 96% of the mesh cells are either hexahedrons or prisms, which are clearly desired, while only 1.6% of the mesh cells are tetrahedrons.

Table 2. Mesh size and quality statistics are given.

Parameter	Value
Minimal edge-length [m]	3.14×10^{-6}
Average edge-length [m]	1.4×10^{-4}
Maximum edge-length [m]	5.9×10^{-3}
Total # of mesh cells	53,512,046
% hexahedrons	80%
% tetrahedrons	1.6%
% prisms	16%
% pyramids	2.5%

Figure 6 shows the mesh resolution on solid surfaces near the front end plate of the bundle, which includes the fuel elements, bearing pads, spacer pads, end plates, and spacer caps. Figure 7 illustrates the mesh in the fluid region between adjacent fuel elements in the bundle. A five-layer inflation zone was generated near the walls of the fuel elements to capture the boundary layer with overall high resolution within the subchannels. Figure 8 shows an enlarged view of the fluid region between two adjacent fuel elements, which also intersects the middle of the spacer pads. This region was most challenging to generate a high quality mesh due to the close proximity of spacer pads, which are also skewed with respect to one another. Note that some of the mesh elements may appear distorted, which is a graphical artifact resulting from the projection of a three-dimensional mesh onto a two-dimensional plane for visualization purposes.

In the rod bundles, the integral scale corresponds roughly to the hydraulic diameter of the channel and the size of the largest eddies, while the dissipation scale is set by viscosity. For the I-LES method, the accurate resolution and propagation of eddies requires a minimum of approximately 4-6 cells per wavelength (eddy). The non-linear, locally-conservative and monotonicity-preserving, advection method provides the transition between the resolved scale and the subgrid scale where dissipation of kinetic energy occurs. Note that the mesh resolution in this work is comparable to similar analyses of subchannel flow in Pressurized Water Reactors by Christon *et al* [23], and is actually finer in some regions with more uniform mesh spacing in smaller subchannels. A grid sensitivity analysis by Christon *et al* [23] demonstrated that while the mean flow behaviour could be reasonably resolved with a medium density mesh, a mesh of approximately double the number of cells was needed to adequately resolve RMS quantities.
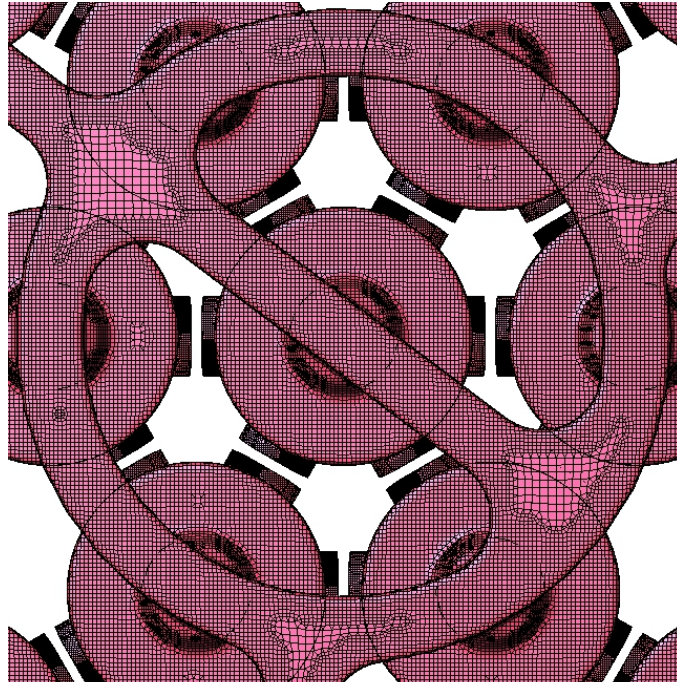
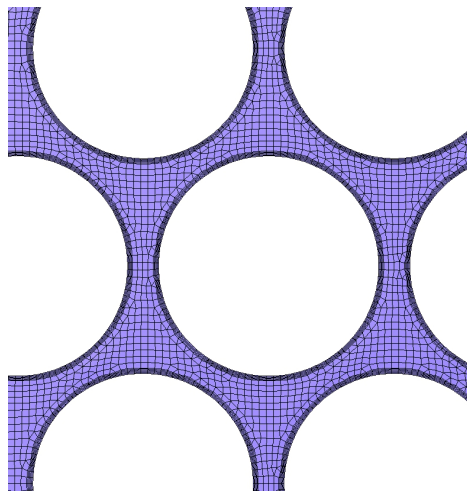**Figure 6.** The computational mesh near the upstream end plate is shown.

Figure 7. The computational mesh is shown through the centre subchannel, which illustrates the high resolution between the fuel elements with a multi-layer inflation zone.
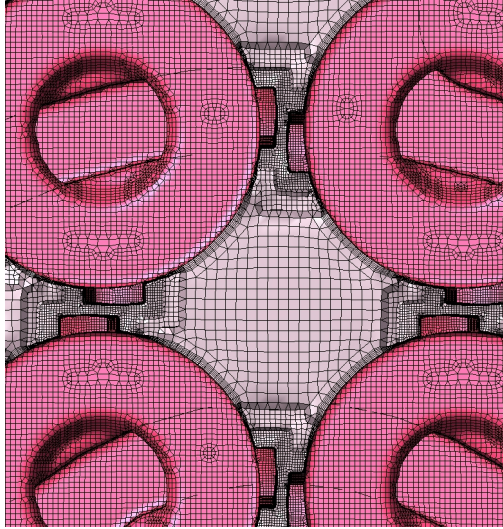
Figure 8. An enhanced view of the computational mesh between four adjacent fuel elements is shown with a five-layer inflation zone (i.e., to better capture the near wall boundary layer), which includes the mesh between contiguous spacer pads.

In general practice of CFD simulations of wall-bounded turbulent flows, the mesh quality along no-slip walls has a significant influence on the accuracy of the numerical solution. Near wall boundary elements need to be small and uniform in order to adequately resolve the flow behaviour near the wall. However, for very complex flow geometries, the size and uniformity of the cells along the wall are difficult to maintain during mesh generation due to the complexity of the geometry. In contemporary CFD engineering practice, the quantity y^+ is commonly used to assess the mesh quality at no-slip walls and represents a dimensionless distance normal to an adjacent wall. The distance from the wall, measured in viscous length units, is defined by

$$y^+ = \frac{y}{v}\sqrt{\frac{\tau_w}{\rho}} \tag{3}$$

where y, v, τ_w, and ρ denote the (dimensional) normal distance from the wall, kinematic viscosity, wall-shear stress, and fluid density, respectively. In this study, the y^+ values were evaluated only for boundaries where there is a no-slip/no-penetration boundary. Although not required by I-LES, normal distance boundary conditions were employed to identify the no-slip/no-penetration walls in the model for the computation of $y+$.

In the mesh study, two different meshes (18M, 54M) were generated by HEXPRESS/HYBRID. The average y^+ monotonically decreased with increasing mesh size. In this paper, the 54M mesh was chosen as the baseline mesh with five boundary layer mesh cells (see Figure 8). The average calculated y^+ value over the fuel bundle surface is close to 1 with a maximum value of 5. The spatial uniformity of the y^+ value is also of importance whereby the spatial distribution of y^+ over the fuel bundle is pretty smooth with small variations of y^+. As y^+ is similar to a local Reynolds-number, the magnitude of the average y^+ value can indicate the relative importance of viscous and turbulent processes in the near wall region. A value of y^+ near approximately 1 is recommended for LES with full wall resolution (i.e., no wall function) [9].

3.3 Solver Details

HYDRA-TH is based on a hybrid projection algorithm for time-dependent, incompressible viscous flow [24]. This hybrid finite element/finite volume algorithm circumvents the usual

divergence stability constraints – such as checkerboard modes in the pressure – and does not require explicit treatment of pressure modes using Rhie-Chow interpolation or a pressure-stabilized Petrov-Galerkin formulation. The hybrid projection algorithm relies on the so-called co-velocity approach, where dual-edge velocities that are centered at unique faces in the grid are made divergence-free and then used for advection. Together with a high-resolution advection scheme with consistent edge-based treatment of viscous/diffusive terms, this yields a robust algorithm for incompressible flows. Here, the second-order (in space and time) accurate projection method is used for the I-LES computations with a fixed CFL automatic time-stepping algorithm. The construction of the high-resolution monotonicity-preserving algorithm with a second-order Trapezoidal rule in time permits an extended stability range. This permits stable, time-accurate I-LES computations with CFL values around 5-10. A maximum CFL value of 4 was chosen here to be conservative.

HYDRA-TH relies on PETSc [25], the ML preconditioner from Trilinos [26], and Hypre [27] for its linear solvers. In particular, Hypre's BoomerAMG is employed as a preconditioner to PETSc's CG solver for the pressure projection linear solve, while the momentum transport linear solve is performed using PETSc's FGMRES solver with PETSc's block Incomplete LU-decomposition as a preconditioner.

3.4   Material Properties and Boundary Conditions

The operating fluid for this particular problem was condensed light water, whereby heat transfer and chemical reactions are not relevant. The fluid was taken to be incompressible and isothermal at 21 °C. The density of water was taken to be 997.2 kg·m^{-3} and the dynamic viscosity is 8.9043×10^{-4} kg·m^{-1}·s^{-1}, which were computed from the Thermalhydraulics Evaluation Package [28]. The inlet was represented as a velocity inlet boundary condition with a uniform axial velocity profile of 0.1191 m·s^{-1}, which is a good approximation to the measured inlet velocity shown in Figure 5.

The outlet face was represented as a pressure outlet boundary condition with a zero gauge pressure applied and all surfaces were treated as solid walls with a no-slip no-penetration boundary condition. Since the I-LES turbulence model was used, turbulent boundary conditions for turbulent kinetic energy and dissipation rate are not required at the inlet. Furthermore, the flow at the inlet of the physical system is fairly laminar, which is due to the design of the pre-conditioning system (i.e., as shown in Figure 2). Turbulence is generated by the separation at the inlet endplate and boundaries in the rod bundle. Here, it was determined that the inflow turbulence intensity was quite low (i.e., <1%) so a uniform velocity profile was used at the inlet. Synthetic turbulence boundary conditions can be required in some forced flow conditions, and for canonical periodic flow in a box where there is not significant energy input due to boundary conditions, only the cascade and subsequent energy decay. The approach used here does seem to be adequate for this particular case, and like other fuel-rod bundle LES simulations, more sophisticated treatments at the inlet were not deemed necessary.

3.5   Convergence Criteria

In this study, the semi-implicit projection time-integration scheme [9] was used to calculate the transient flow characteristic over the complex wall-bounded flow channel. The basic philosophy of the projection method is to provide a legitimate way to decouple the pressure and velocity fields to provide an efficient computational method for transient incompressible flow simulations. Time integration was dynamically determined by HYDRA-TH to constrain the maximum CFL number to 4, which resulted in a step size of approximately 10^{-4} s for most of the simulation (see Figure 9). The domain integrated kinetic energy, $\int \frac{\rho v^2}{2} d\Omega$, was computed by HYDRA-TH with respect to time, which is also shown in Figure 9. Here, Ω denotes the volume of the fluid domain. Based on these calculations, a time of 2 s was selected as the starting point for calculating time-integrated statistics

until the end of the simulation at 10 s. This time interval corresponded to approximately 70,000 time steps. The initial 2 s corresponds to the startup time required to establish the turbulent boundary layers, after then, the volume-integrated kinetic energy has reached a statistically stationary state. Convergence at the time step level was determined by ensuring that the residuals of all three-momentum equations and the continuity equation were less than 10^{-5}. In addition, the outlet flow rate was monitored to ensure that continuity was satisfied as the simulation progressed.
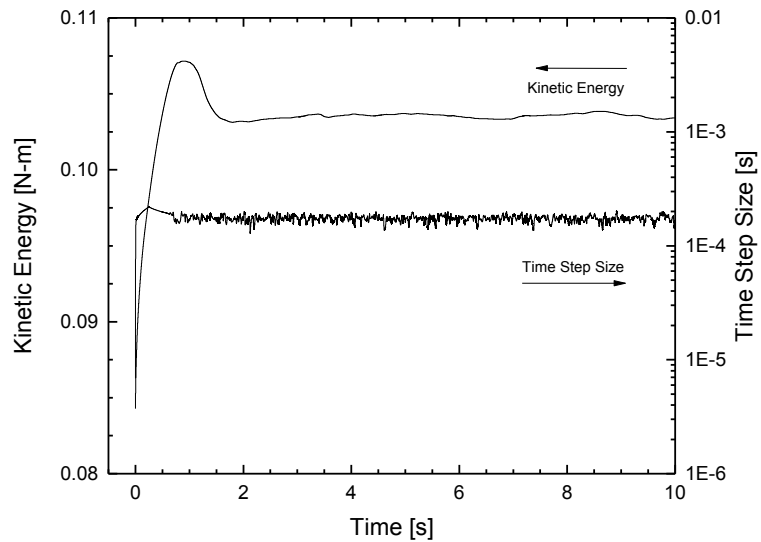
Figure 9. The computed volume-integrated kinetic energy is plotted with respect to time for the HYDRA-TH simulation, which was used to determine when temporal statistics should be recorded. Also, the time step size is superimposed using the same abscissa.

Figure 10 plots the instantaneous axial velocity at a particular node located immediately downstream from the front end plate. Since the flow is still numerically developing in the first few seconds, results should only be considered after ~2 s. The time averaged axial velocity from 2 to 10 s and standard deviation are superimposed on Figure 10. These results were used to determine whether the simulation has reached a stage of statistically stationary flow.
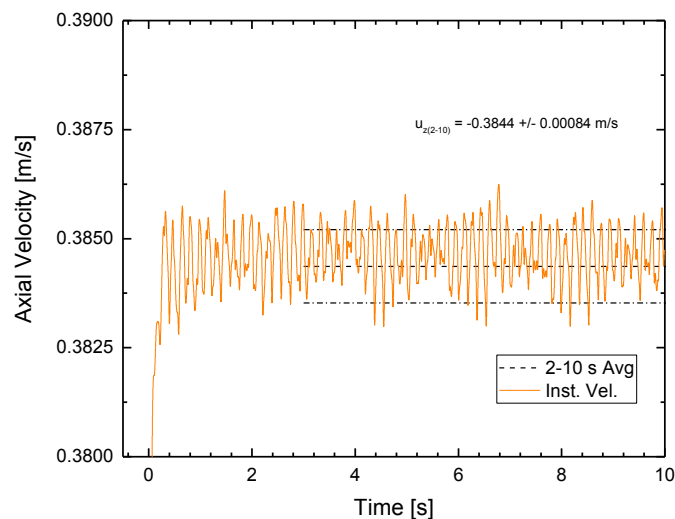

Figure 10. The predicted instantaneous axial velocity is plotted for a particular node located immediately downstream from the front end plate.

14

4   Presentation and Discussion of Results

The space between neighbouring fuel elements in a CANDU fuel bundle is termed a subchannel, through which the coolant is flowing. For good convective heat transfer, highly turbulent, thin velocity boundary layers and a high fluid velocity are advantageous. Inter-subchannel mixing improves the homogenization of coolant temperature within a CANDU fuel bundle, thus promoting the normalization of fuel element temperatures.

By subdividing the fuel bundle into four concentric subchannel regions (normally referred to as "subchannel rings") and calculating the cross-sectional averaged streamwise velocity and the cross-sectional integrated flow rates in these regions, insights about the flow distribution can be achieved. Figure 11a shows the four subchannel regions with the outer diameters indicated in millimeters. Each subchannel ring is assigned a certain colour (i.e., red, light blue, green and dark blue) and name (i.e., A1-A4), which is used to indicate the corresponding regions in Figure 11b and c. Axial positions that are highlighted with light orange have to be considered carefully, due to abnormalities in the acquisition process. In Figure 11b, the cross-sectional averaged streamwise velocity relative to the overall average of the streamwise velocity (i.e., bulk fluid velocity) is depicted for the four subchannel rings. Throughout the length of the fuel bundle, the average U_z velocity in A1 is considerably lower than the remaining three subchannel rings; A2 and A3 are fairly consistent and roughly equal to the bulk velocity, and A4 is slightly below the bulk velocity. As to be expected, all four regions begin with roughly the same value at the beginning of the bundle (i.e., Z = 0 mm). Afterwards, the flow through A4 decreases while A3 increases. Around the middle of the bundle, where the strongest cross-sectional obstruction due to spacer and bearing pads is present, considerable mixing among all four subchannel rings takes place. Hence, the bundle appendages lead to a velocity re-distribution, which is positive for A2 and A4, but negative for A1 and A3.

The average streamwise velocities in A1 and A4 decrease throughout the length of the fuel bundle, whereas the average streamwise velocity in A2 and A3 marginally increase as the fluid progresses downstream. A possible explanation may be the increasing velocity boundary layer thickness, which progressively affects fluid flow in subchannel ring A1. In addition, adjacent fuel elements are in much closer proximity to one another in A1 in comparison to the remaining subchannel rings. Indeed, this matter is quite important in terms of the coolability of the central fuel rod.

The integrated flow rate for each of the four subchannel rings is plotted in Figure 11c as a percentage of the bulk flow rate. As a form of verification, the sum of flow rates calculated from A1 to A4 is displayed as a dashed line, which is very near 100%. As is shown in Figure 11c, ~40% of the fluid flow rate is accommodated by subchannel ring A3, ~30% in A4, ~20% in A2 and finally ~10% in A1. The graphs demonstrate similar behaviour as previously discussed for the relative cross-sectional averaged streamwise velocity.

Another region of interest is immediately upstream from the bundle (i.e., Z < 0 mm). The flow rates and average streamline velocities in subchannels A1-A3 are initially high and decrease over the front end plate, whereas region A4 experiences the opposite trend. This is due to the sudden cross-section reduction starting with the front end plate, where the flow has to evade the downstream obstruction. For A1 to A3, the flow has to funnel through the small openings of the end plate. On the pressure tube wall upstream from the fuel bundle, a significant velocity boundary layer has developed. Hence, the flow can evade into these regions and reduce the velocity boundary layer again. This is also the reason why the flow rate increases for A4 just downstream from the front end plate.

A general conclusion that can be drawn from these results is that all four subchannel rings are able to communicate with each other. With appropriate passive flow control devices (e.g., vanes), a redistribution of the flow is possible. For the given CANDU fuel bundle, this is already partially achieved by the spacer and bearing pads. The flow through subchannel A1 and around the central

element in particular is quite important since the average streamwise velocities are up to 30% lower than the bulk velocity. When assuming constant material properties, this also implies that the Reynolds number is reduced. Fortunately, the neutron flux is the lowest in the central region of the fuel bundle, which results in the lowest local linear power within the bundle [10]. Thus, the reduced coolability resulting from a lower flow rate through subchannel ring A1 is partially offset by the lower neutron flux.
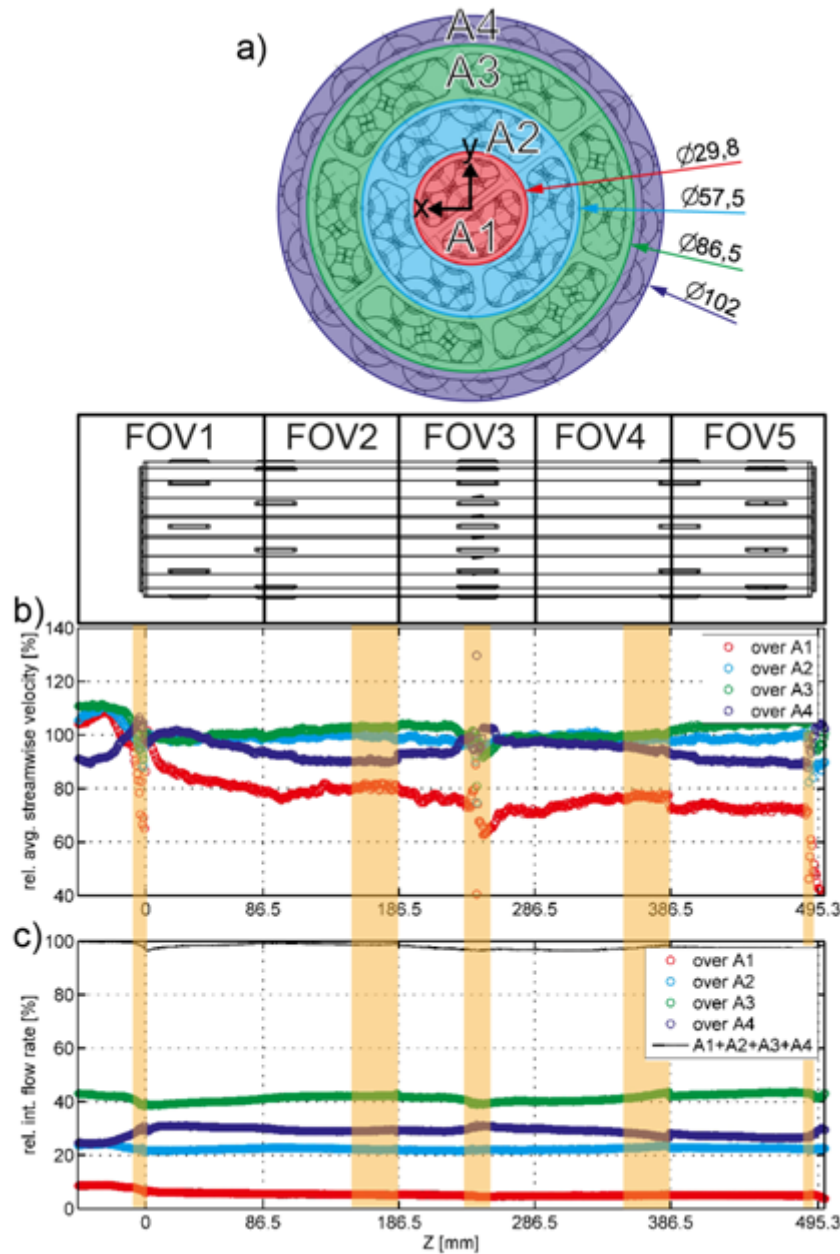

Figure 11. a) Front view of a CANDU fuel bundle depicting the four subchannel integration areas; b) Cross-sectional integrated measured streamwise velocity represented relative to the bulk streamwise velocity; c) Cross-sectional integrated measured flow rate relative to the total flow rate through the channel. Erroneous areas are marked with an orange bar. Graphic adapted from Wassermann [11].

The distribution of the streamwise velocity component U_z for different axial positions is considered in consecutive contour plots in Figure 12. Starting with $Z = -10$ mm, the flow upstream from the front end plate is very homogeneous with a small boundary layer at the pressure tube wall. This figure verifies using a constant axial velocity as a boundary condition at the inlet. For $Z =$

10 mm, a flow field has developed in each subchannel, where the maximum velocity values are present in area A1. In all other areas, U_z is evenly distributed. Only small boundary layers surrounding the elements and at the pressure tube wall are visible (i.e., roughly the size of a voxel or smaller). Effects resulting from the obstruction of the front end plate are still observed in the flow field downstream. Following the contour plots further downstream (i.e., Z = 50 mm, Z = 100 mm and Z = 200 mm), the maximum velocity values increase in the subchannel rings A2 to A4 and decrease in A1. This behaviour was also observed in Figure 11. Concurrently, the boundary layers increase in size to a greater degree in some subchannels than others. In the middle of the bundle at Z = 250 mm, the maximum streamwise velocities in the entire flow field develop. The cross-sectional area is a minimum in the middle of the bundle (i.e., Z = 250 mm) due to the presence of the bearing and spacer pads.

The last contour plot in Figure 12 (i.e., Z = 500 mm) shows the streamwise velocity distribution approximately 5 mm downstream from the rear end plate. There is significant recirculation following the ribs of the rear end plate, which would enhance mixing downstream. Behind the radial struts of the rear end plate, large wakes with recirculating fluid are present. Additionally, jets with high-speed fluid develop from the subchannels of areas A2 to A4. In comparison, fluid velocities in the centre area (i.e., A1) are relatively low. One critical result of such a flow profile could be fluid-structure interactions.

In a commercial CANDU reactor, multiple bundles are placed in series within a fuel channel, whereby the flow downstream of one bundle is affected by the presence of the adjacent downstream bundle. Indeed, the presence of neighbouring fuel bundles complicates flow between the two adjacent bundles, particularly since fuel bundles may not be circumferentially aligned with one another. This could lead to increased mechanical loads on the front end plate and fuel element heads. Another potential scenario resulting from the uneven out-flow profile and the complex interaction with the entry region of the downstream fuel bundle would be the undersupply of certain subchannels with coolant flow. As shown above, a fluidic interaction between the subchannels in angular and radial positions is possible. Nevertheless, the redistribution of coolant in the radial direction is not very intensive.

As the CANDU fuel bundle has a certain rotational symmetry, it is valuable to transform the cross-stream velocity components into a radial velocity U_R and an angular velocity U_Φ. This enables the observation of flow redistribution in the radial direction, which is associated with fluid movement from one subchannel ring to a neighbouring region. With U_Φ, a swirling motion or a fluid movement within a subchannel ring is identifiable. Figure 13 depicts different contour slices showing the U_R and U_Φ fields for critical axial positions before and after the front end plate and in the presence of the spacer pads. The displayed coordinate system gives the direction for U_R and U_Φ.

For Z = -5 mm, the U_R plot shows that the flow is affected by the front end plate and the presence of the fuel bundle. The radial redistribution of the flow is the highest for area A4 in the positive R-direction. This redistribution was observed for the flow rate integration over subchannel ring A4 in Figure 11. The radial movement in the negative R-direction is only slightly visible. In addition, U_Φ depicts the detection produced by the radial struts of the front end plate. The angular detection is much weaker than the radial detection.

The contour plots for Z = 5 mm show strong interaction between the radial subchannel rings. The radial velocity reaches a maximum right after the small gaps of each ring. Like before, the radial movement in the positive radial direction is greater than in the negative direction. Referral to the U_Φ plot for this Z-location shows that high angular velocity values are only present where the radial struts are located upstream. Another critical Z-location is the region where the spacer pads are located, which corresponds to Z = 242 mm. Again, strong radial movement (especially from A3 to A4 and A1 to A2) is present. At positions where spacer pads are present and the streamwise velocity value is

high, increased angular movement is observable. This is mainly present in the third subchannel ring A3.
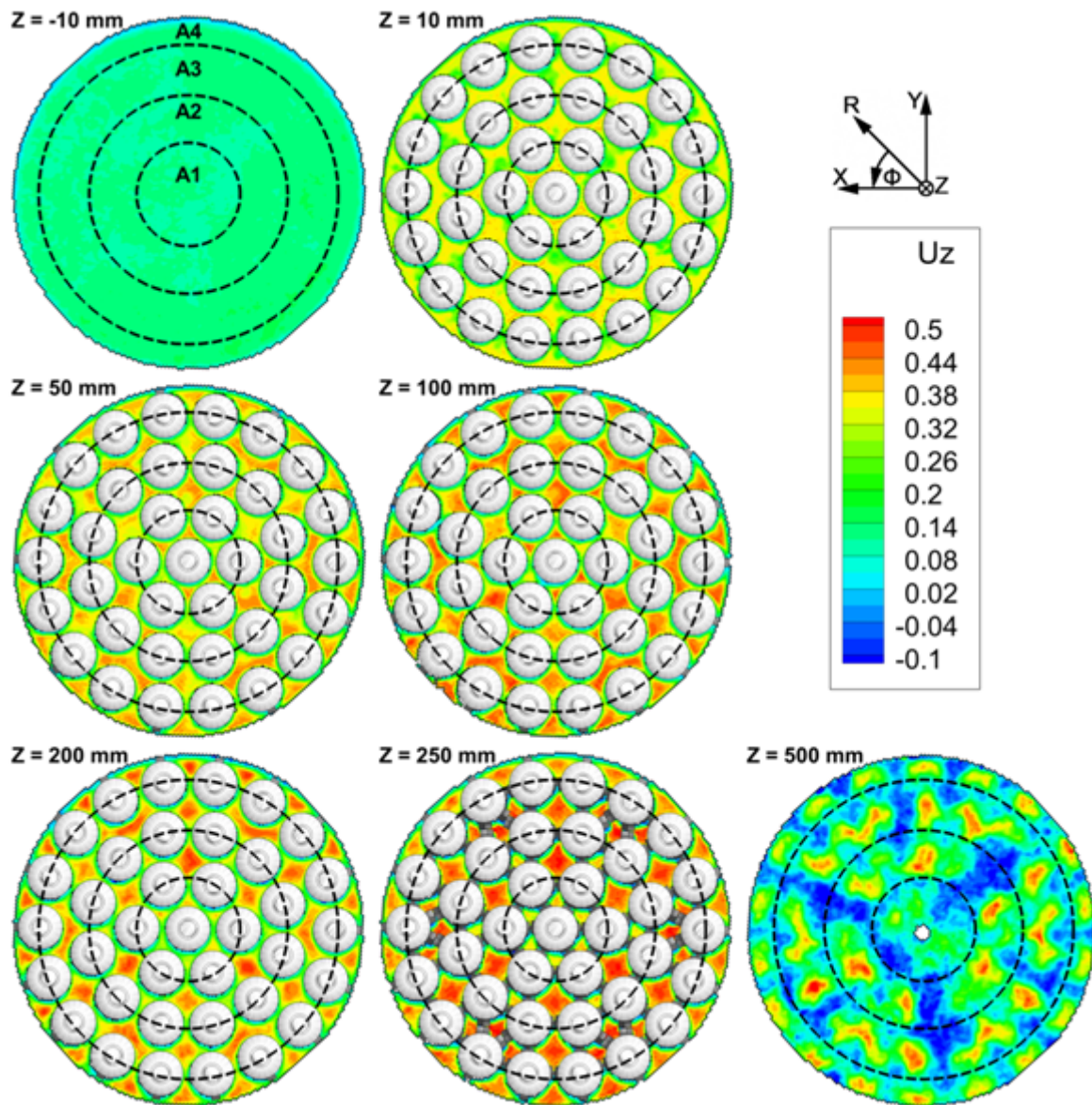

Figure 12. Measured axial velocity contour plots are shown at various axial positions. The dashed concentric rings represent the different subchannels A1-A4. Graphic adapted from Wassermann [11].
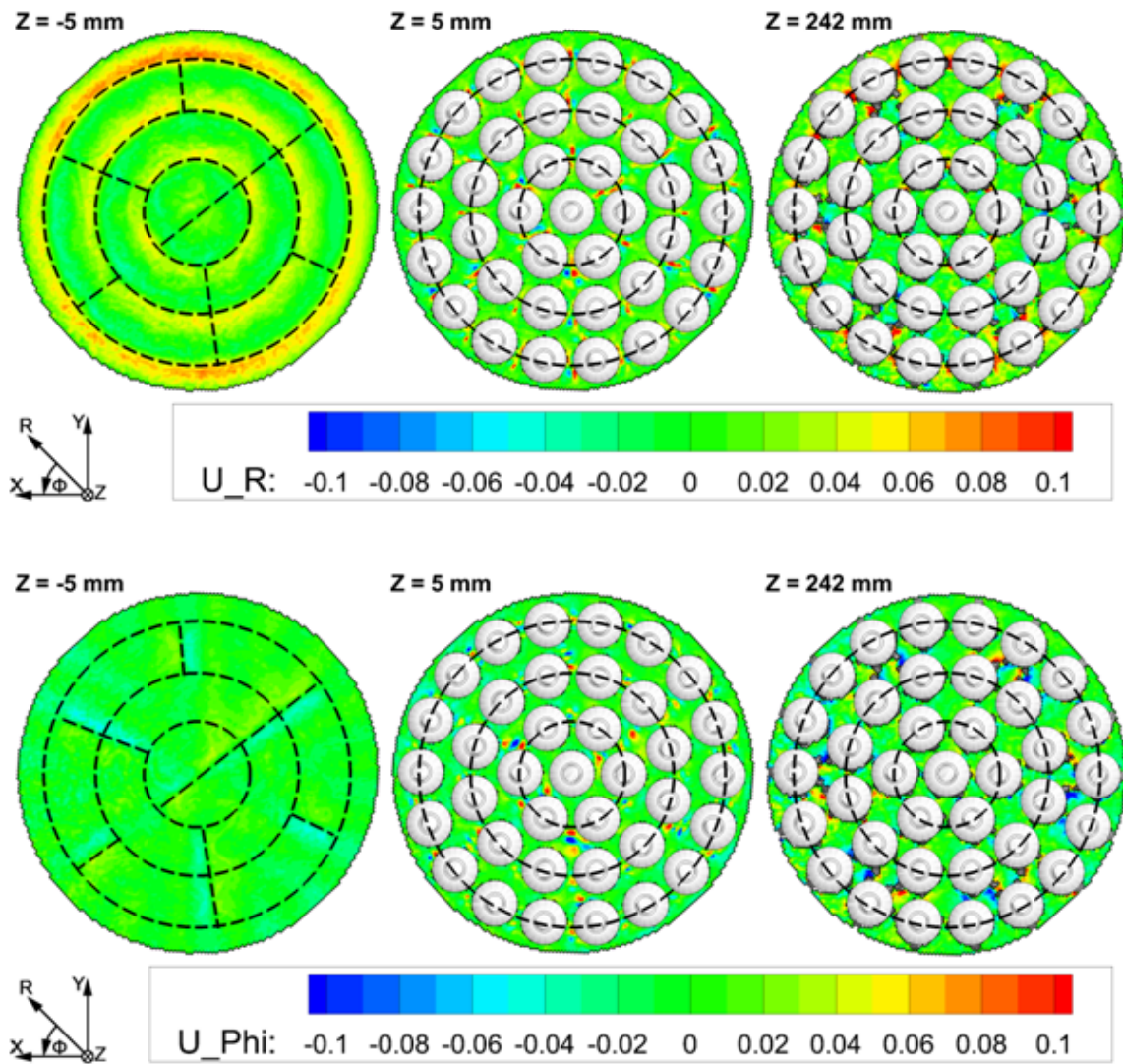
Figure 13. Contour plots of the measured radial (U_R) and angular (U_Φ) velocity components along various axial positions. The dashed concentric rings represent the different subchannels A1-A4. Graphic adapted from Wassermann [11].

Figure 14 gives a qualitative comparison of predicted and measured axial velocity distributions throughout the fuel bundle at axial positions of 10 mm, 50 mm and 250 mm downstream from the front end plate. The contour plots shown at 10 mm are consistent with Figure 11, whereby the axial velocity is fairly well distributed amongst the subchannels. At an axial distance of 10 mm, the flow is clearly still developing, as evidenced by the non-uniform velocity distributions in Figure 14, which are consistent between both experiments and simulations.

As the fluid progresses downstream, the flow begins to develop with more evident velocity peaks. Also, it is clear that the majority of flow takes place in subchannel rings A2 and A3. Axial velocities experience a maximum at the centre of the bundle (i.e., near 250 mm) where the fluid regime is constricted due to a smaller cross-sectional area. Again, this is due to the presence of bearing and spacer pads, as shown in Figure 1. This figure also clearly demonstrates the relatively higher fluid velocity through subchannel rings A2 and A3 compared to A1 and A4. Note that the near-zero fluid velocity regions in the predicted contour plot at $Z = 50$ mm is due to the presence of bearing pads that alternate positions near the front of the bundle, which is consistent with the measured values shown in the adjacent plot. The position of bearing pads on the fuel bundle is shown in Figure 1.
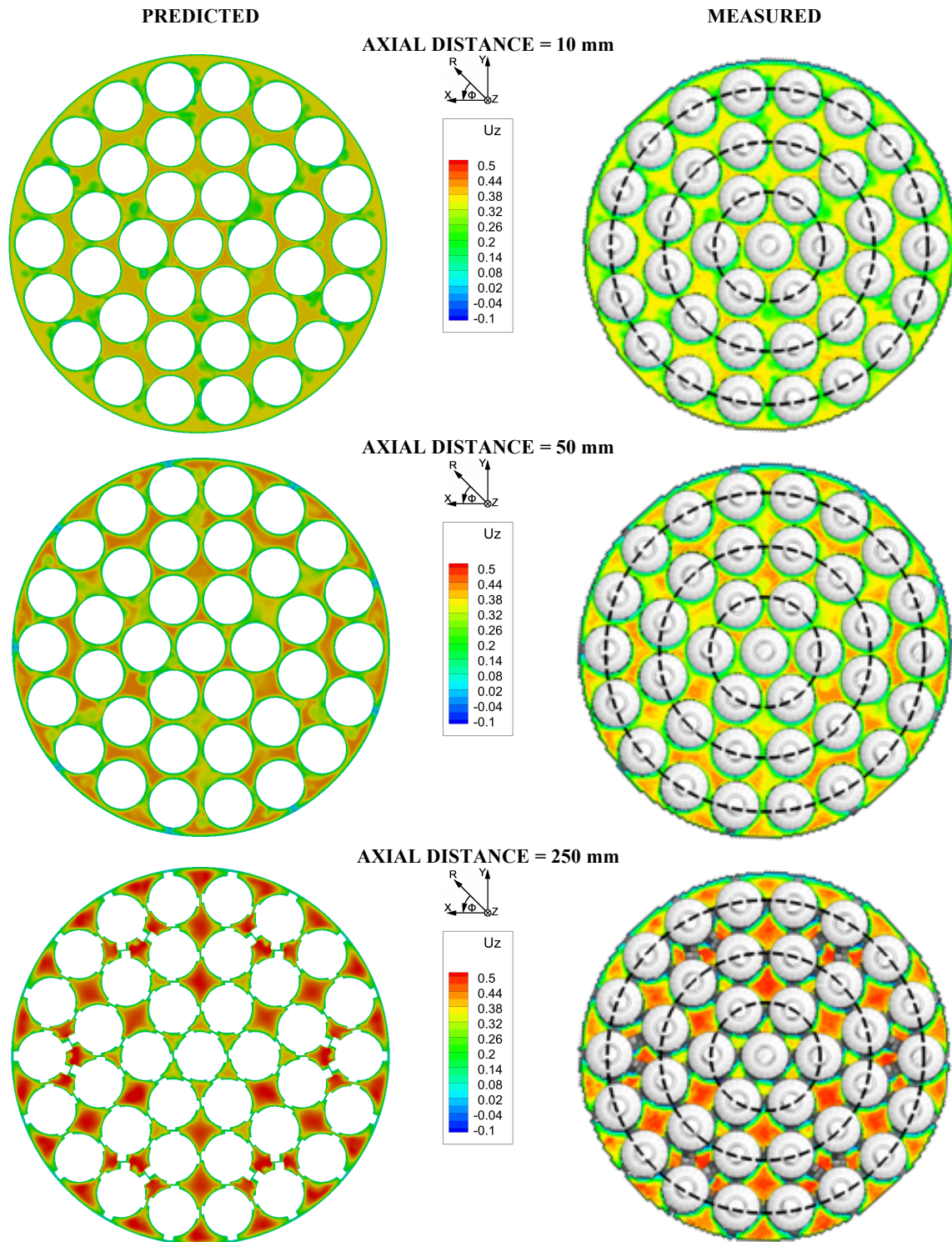
AXIAL DISTANCE = 10 mm

AXIAL DISTANCE = 50 mm

AXIAL DISTANCE = 250 mm

Figure 14. Measured and predicted axial velocities are qualitatively compared at various axial positions in the domain.

Figure 14 demonstrates very good qualitative agreement between measured and predicted axial velocity contours, while Figure 15 gives a quantitative comparison along both horizontal and vertical directions at 5, 10, 50 and 250 mm axial distances. Figure 16 identifies the horizontal and vertical directions superimposed on a cross-sectional view of a fuel bundle, which should be used in the context of Figure 15. In general, there is very good agreement between measured and predicted axial velocity quantities. Not only are trends in axial velocity profiles well represented, but so are absolute values.
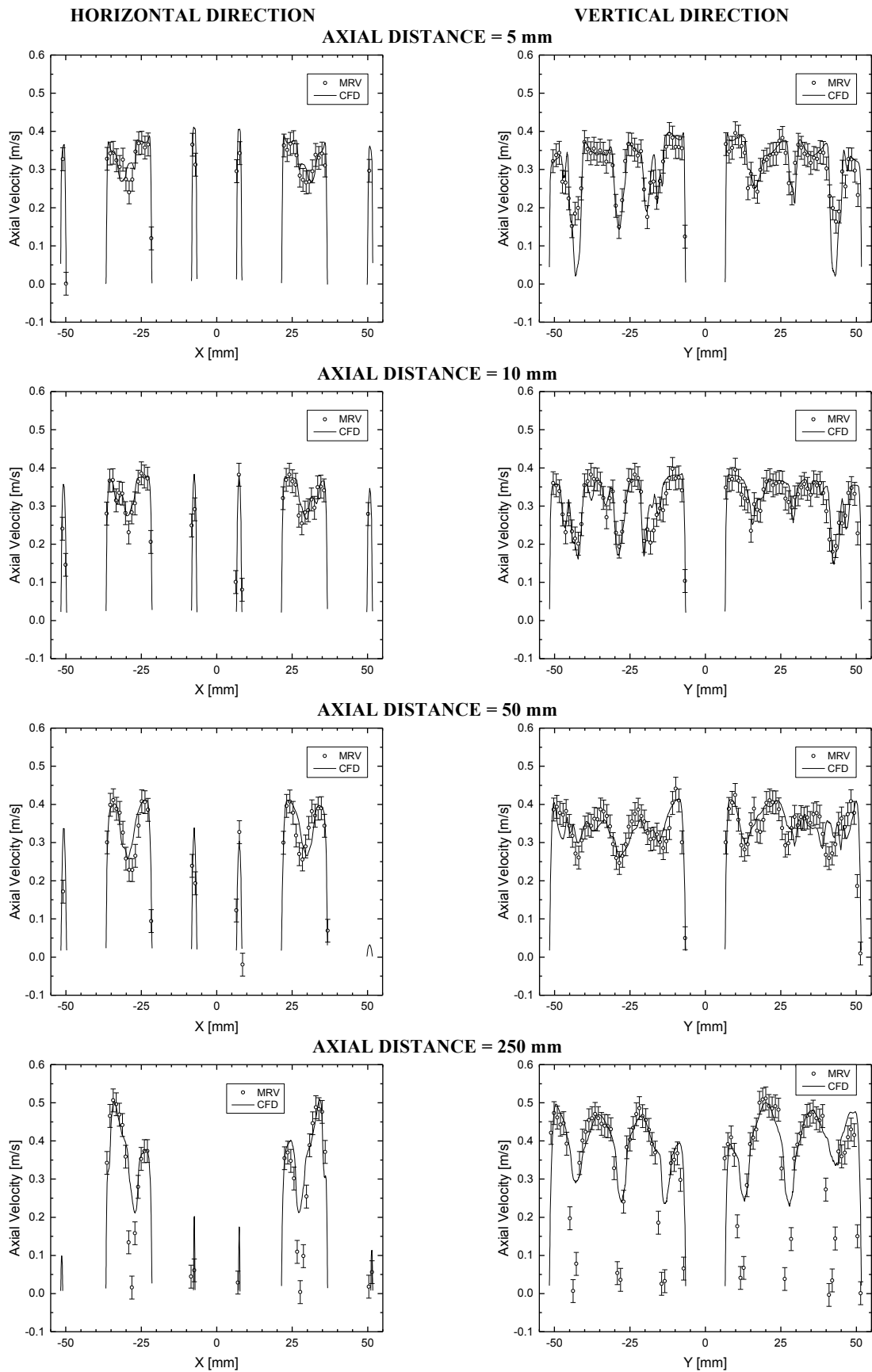
HORIZONTAL DIRECTION　　　　　　　　**VERTICAL DIRECTION**

AXIAL DISTANCE = 5 mm

AXIAL DISTANCE = 10 mm

AXIAL DISTANCE = 50 mm

AXIAL DISTANCE = 250 mm

Figure 15. Measured and predicted axial velocities are quantitatively compared at various axial positions in the domain. The orientations of horizontal (i.e., X) and vertical (i.e., Y) directions are illustrated in Figure 16.
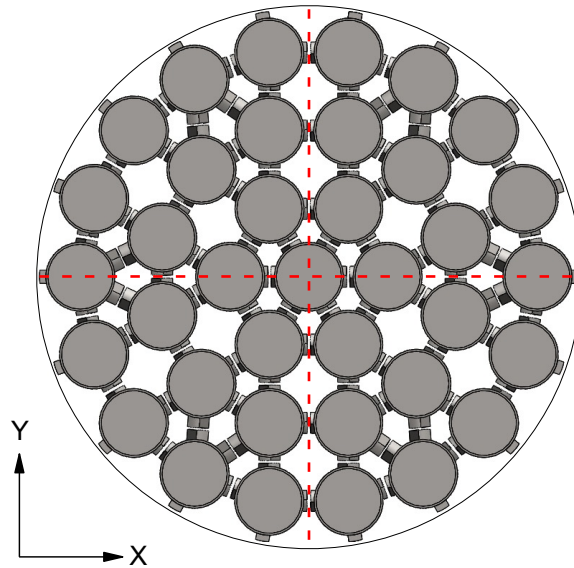
Figure 16. Cross-sectional view of the mid-plane of a fuel bundle indicating
the vertical and horizontal directions used in Figure 15.

As is shown in Figure 15, recirculation shortly downstream from the front end plate (i.e., $Z = 5$ mm) appears to be more pronounced in the CFD simulation in the vertical direction in comparison to the MRV measurements. Conversely, recirculation is predicted to be lesser in the horizontal direction. Although these discrepancies are fairly minor and are not of great concern, they are most likely due to the misrepresentation of small eddies in the simulation near the front end plate, whereby a large degree of recirculation takes places, since they are modelled rather than resolved.

Predicted and measured axial velocity profiles further downstream at 10 and 50 mm are in very good agreement with one another. Conversely, the discrepancy between measured and predicted values near the middle of the bundle (i.e., $Z = 250$ mm) is quite noticeable. The MRV measurements suggest that there are multiple stagnation zones near the midplane, which does not make sense because there is no physical reason why the flow should stagnate in this region. This may be due to the relatively larger experimental error in this region (as is shown in Figure 7), which is likely due to insufficient voxel resolution between adjacent fuel elements.

Figure 17 illustrates a series of predicted isosurface plots of pressure at various regions of the fuel channel. Note that separation zones near the bearing pads are predicted. Furthermore, the fluid pressure isosurface at the downstream end plate shows a very complex structure, which results in considerable recirculation in this region and was observed experimentally in Figure 12. Large pressure gradients are shown in the downstream region, particularly near the interface of fuel elements and the end plate. The largest pressure gradients appear in subchannel rings A2 and A3.
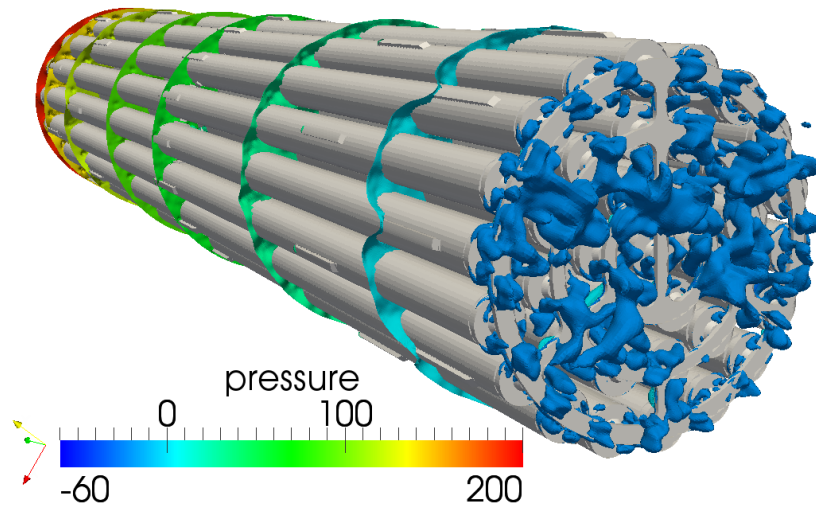
Figure 17. Predicted pressure isosurface plots are shown in the downstream region of the bundle. In this figure, fluid flows from left to right alongside the fuel rods.

Helicity isosurface plots are illustrated in Figure 18. As to be expected, small helical structures are formed near the leading edges of bearing pads and trail downstream. Also, a significant number of helical structures are observed at the downstream end plate resulting from the complex structure of the rear end plate. The complex behaviour immediately downstream from the rear end plate demonstrated by the pressure and helical isosurface plots suggest even more complex behaviour if two fuel bundles are adjacent to one another.

The helical structures are very intense in the region adjacent to the upstream end plate. In this area, turbulence and fluid mixing is very strong. After a short distance downstream from the front end plate, the helical structures disappear again. This is an effect of flow acceleration that is caused by the flow obstruction of the front end plate. In this region, the helical structures are stretched in the Z-direction and are ultimately dissipated. This is analogous to the effect of a nozzle. This is disadvantageous for heat transfer as laminar flow has no fluid mixing and an increased boundary layer thickness. A counter measure for that would be to induce helical structures using passive flow control devices as for instance discussed by Yao [29]. This would increase the flow rotational momentum and lead to increased fluid mixing and a reduction of the velocity boundary layer.
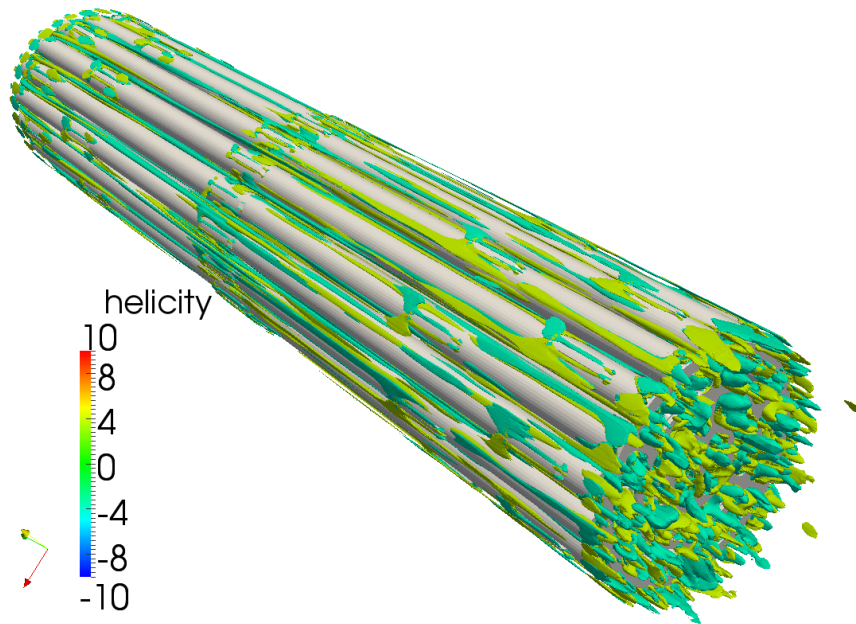
Figure 18. Predicted helicity isosurface plots are shown.

Under abnormal conditions that differ from what has been described heretofore, debris may be circulating in the Primary Heat Transport System (PHTS) and get lodged somewhere in the fuel channel, potentially resulting in a partial blockage of a subchannel. Consequently, the adjacent fuel elements in these subchannels would suffer from insufficient cooling with the increased likelihood of fuel failure, whereby the primary concern would be the release of radioactive fission products to the PHTS. During one of the MRV experimental campaigns, a suspicious velocity distribution led to the discovery of debris lodged within the bundle, which is shown in Figure 19. The source of this debris is believed to be non-sintered polyamide powder, which is likely to stick between narrow gaps. Although at the time it appeared that the presence of this debris was undesirable, this discovery came to the realization of the valuable capability of MRV to not only perform velocity measurements, but to also verify that the fluid regime that is being measured is free of any such obstructions, which is not possible with any other experimental technique. Moreover, MRV is able to quantify the effects of such debris on the local flow field, which is quite advantageous to investigate abnormal conditions in-reactor.
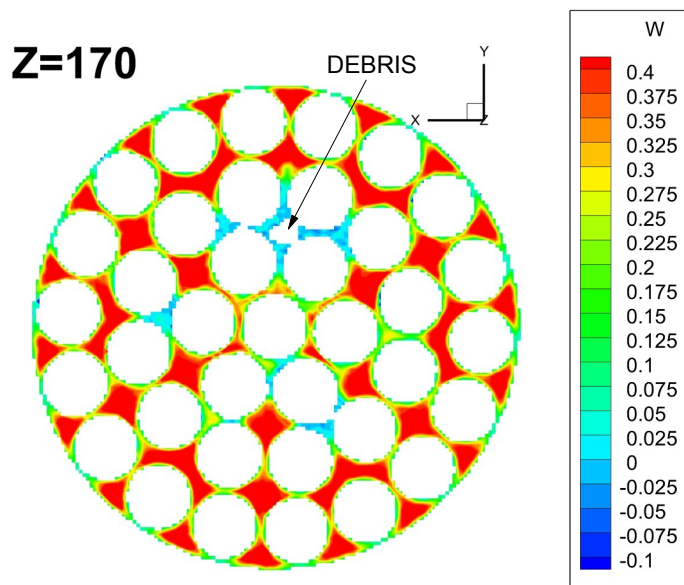
Figure 19. In a separate experiment, MRV measurements revealed debris lodged
within the bundle and the resulting effects on the local flow field.

The experimental and computational analyses described herein of flow through a 37 element CANDU fuel bundle were generally in very good agreement with one another. One of the main reasons why the numerical analysis is in such great agreement to the corresponding measured values is because of the high level of fidelity captured by the I-LES turbulence model. However, the use of this model comes at a great computational cost. The final simulation of the 54 million cell mesh was executed for ~110,000 time steps on the Institutional Computing High Performance Computing platform at the Los Alamos National Laboratory with approximately 2000 cores for 14 days. Indeed, this places such an analysis in the realm of research and development, which is not compatible with direct industrial use at this time.

One potential industrial application of the combined experimental and computational approach described herein could investigate the modified 37 element bundle design – known as the 37M bundle – designed by Ontario Power Generation for the Darlington Nuclear Generating Station. This design is essentially identical to what is shown in Figure 1 except that the centre fuel element has a smaller diameter in the 37M design. The motivation of this design change was to increase flow surrounding the central element where dryout is expected to initially occur during a postulated accident scenario [30]. Increasing flow near this element restores some of the lost safety margin due to reactor ageing [30]. The foregoing capabilities could be applied to measure and predict local flow conditions for this design and other similar design changes that may be considered in future investigations.

Although the flow conditions considered in these analyses are not representative of in-reactor conditions – specifically, lower temperature, hydrostatic pressure and mass flow rate – progress has been made in gaining confidence in the combined experimental and computational approach. For instance, three-dimensional, three-component velocity measurements within a CANDU fuel bundle have not been possible until now without the use of MRV technology. Also, numerical simulations have demonstrated the ability to predict detailed flow distributions in a very complex geometry. Future investigations are anticipated to study the effects of flow-bypass resulting from a crept pressure tube and conjugate heat transfer simulations that are representative of in-reactor conditions. Also, future work may include developing the capability to distinguish between velocity and density information of gas and liquid phases in every voxel in a time-averaged manner for two phase flows.

5   Conclusions

Progress has been made in developing the capability of investigating fluid flow through a 37 element CANDU fuel bundle through experimental and computational means. Experiments performed with MRV provide three-dimensional, three-component fluid velocity measurements without intruding the flow, introducing tracer particles or requiring optical access of the flow field. CFD simulations performed with HYDRA-TH using the I-LES turbulence model were in very good agreement with the foregoing experiments. Although these investigations were performed at much lower Reynolds numbers than what is experienced in-reactor, these analyses demonstrate for the first time the capability of measuring inter-subchannel mixing, particularly in regards to quantifying the effects of turbulence induced mixing from the appendages. Moreover, the capability of verifying the absence (or presence) of debris from internal fluid flow measurements has been demonstrated, which is an invaluable feature to ensure reliable fluid velocity measurements. The development of this combined experimental and computational capability instills confidence in understanding the complex behaviour of fluid flow through a fuel bundle, which has important implications to performance and safety.

Appendix

A mesh sensitivity analysis was performed to determine the sensitivity of CFD simulation results on mesh resolution. In addition to the mesh shown in section 3.2, which was mainly developed based on experience with subchannel flow simulations, a coarse mesh was generated using HEXPRESS/HYBRID with the same geometry and formulation. The main difference between the two meshes is that three inflation zones were used in the coarse mesh instead of five, and the base mesh size was increased to achieve a total mesh count of 18 million cells (rather than 54 million for the fine mesh). HEXPRESS/HYBRID applied the same refinement techniques (e.g., near the appendages, near neighbouring wall surfaces) for both meshes, which is a function of the base mesh size.

Figure 20 compares axial velocity predictions along the horizontal and vertical directions at an axial position of 5 mm between both meshes. This particular axial position was selected because it is shortly downstream from the front end plate, where the flow is expected to experience an appreciable degree of turbulence. Generally, axial velocity predictions are fairly comparable between the two simulations with exception of some of the subchannel regions in the vertical direction. Simulation results from the fine mesh are considered well resolved, especially when considering that the total number of cells is three times greater than the coarse mesh.
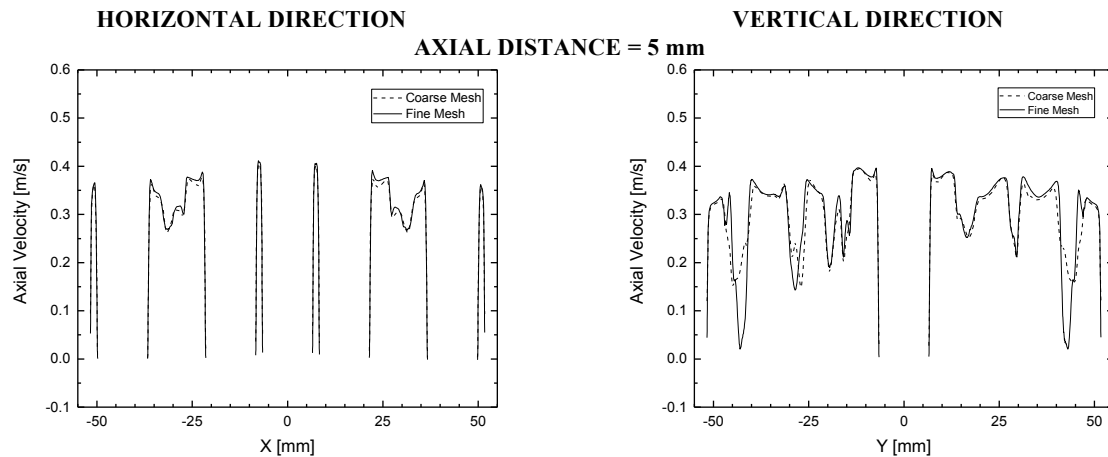
HORIZONTAL DIRECTION   VERTICAL DIRECTION
AXIAL DISTANCE = 5 mm

Figure 20. Axial velocity predictions produced from a coarse and fine mesh are compared along the horizontal and vertical directions at an axial position of 5 mm.

References

1. B.N. Hanna, "CATHENA: A Thermalhydraulic Code for CANDU Analysis," *Nuclear Engineering and Design*, 180 (1998) 113-131.
2. Y.F. Rao and N. Hammouda, "Recent Development in ASSERT-PV Code for Subchannel Thermalhydraulics", *Proceedings from the 8th International Conference of CANDU Fuel*, Honey Harbour, Canada (2003).
3. K. Podila and Y.F. Rao, "CFD Analysis of Flow and Heat Transfer in Canadian Supercritical Water Reactor Bundle", *Annals of Nuclear Energy*, 75 (2015) 1-10.
4. M.H.A. Piro, F. Wassermann, S. Grundmann, B.W. Leitch and C. Tropea, "Progress in On-Going Experimental and Computational Fluid Dynamic Investigations within a CANDU Fuel Channel", *Nuclear Engineering and Design*, 299 (2016) 184-200.
5. M.A. Bernstein, Handbook of MRI pulse sequences, Academic Press, Boston (2004).
6. M. Markl, M.T. Draney, M.D. Hope, J.M. Levin, F.P. Chan, M.T. Alley, N.J. Pelc and R.J. Herfkens, "Time-Resolved 3-Dimensional Velocity Mapping in the Thoracic Aorta: Visualization of 3-Directional Blood Flow Patterns in Healthy Volunteers and Patients", *Journal of Computer Assisted Tomography*, 28(4) (2004) 459-468.
7. C.J. Elkins and M.T. Alley, "Magnetic Resonance Velocimetry: Applications of Magnetic Resonance Imaging in the Measurement of Fluid Motion", *Experiments in Fluids,* 43 (2007) 823-858.
8. S. Grundmann, F. Wassermann, R. Lorenz, B. Jung and C. Tropea, "Experimental Investigation of Helical Structures in Swirling Flows", *International Journal of Heat and Fluid Flow*, 37 (2012) 51-63.
9. M.A. Christon, "Hydra-TH Theory Manual", In Tech. Rep. LA-UR 11-05387, Los Alamos National Laboratory (2011).
10. R.D. Page, "Canadian Power Reactor Fuel," Atomic Energy of Canada Limited, Technical Report AECL 5609 (1976).
11. F. Wassermann, "Magnetic Resonance Imaging Techniques for Thermofluid Applications" PhD Dissertation, Technische Universität Darmstadt, Germany (2015).
12. F. Testud and M. Zaitsev, *Proceedings from the 17th Annual Meeting of the International Society for Magnetic Resonance in Medicine*, Honolulu, Hawai'i, USA (2009) 2791.

13. D. McRobbie, E.A. Moore, M.J. Graves and M.R. Prince, *MRI from Picture to Proton*, Cambridge University Press (2002).
14. J. Bakosi, M.A. Christon, R.B. Lowrie, L.A. Pritchett-Sheats and R.R. Nourgaliev, "Large-Eddy Simulations of Turbulent Flow for Grid-to-Rod Fretting in Nuclear Reactors," *Nuclear Engineering and Design*, 262 (2013) 544-561.
15. A. Bhattacharya, S.D. Yu and G. Kawall, "Numerical Simulation of Turbulent Flow Through a 37-Element CANDU Fuel Bundle", *Annals of Nuclear Energy*, 40 (2012) 87–105.
16. F. Abbasian, S.D. Yu and J. Cao, "Experimental and Numerical Investigations of Three-Dimensional Turbulent Flow of Water Surrounding a CANDU Simulation Fuel Bundle Structure Inside a Channel", *Nuclear Engineering and Design*, 239 (2009) 2224–2235.
17. A. Zaretsky, "Simulation of Intersubchannel Mixing in a Triangular Nuclear Fuel Bundle Geometry," MSc. Thesis, McMaster University, Hamilton, Canada (2014).
18. F.F. Grinstein, L.G. Margolin and W. Rider, *Implicit Large Eddy Simulation: Computing Turbulent Fluid Dynamics*, Cambridge University Press, 2007.
19. M.A. Christon, M.J. Martinez and T.E. Voth, "Generalized Fourier Analysis of the Advection-Diffusion Equation – Part I: One-Dimensional Domains," *International Journal Numerical Methods in Fluids*, 45 (2004) 839-887.
20. T.E. Voth, M.J. Martinez and M.A. Christon, "Generalized Fourier Analysis of the Advection-Diffusion Equation – Part II: Two-Dimensional Domains," *International Journal Numerical Methods in Fluids*, 45, (2004) 889–920.
21. SolidWorks Corporation, "SolidWorks User's Guide" (2015).
22. Numeca Inter., HEXPRESS/Hybrid User Manual, Version 11 (2014).
23. M.A. Christon, R. Lu, J. Bakosi, B.T. Nadiga, Z. Karoutas, M. Berndt, *Journal of Computational Physics*, 322 (2016) 142-161.
24. M.A. Christon, J. Bakosi, B.T. Nadiga, M. Berndt, M.M. Francois, A.K. Stagg, Y. Xia, H. Luo, "A Hybrid Incremental Projection Method for Thermal-Hydraulics Applications," *Journal of Computational Physics*, 317 (2016) 382-404.
25. S. Balay, S. Abhyankar, M. Adams, J. Brown, P. Brune, K. Buschelman, L. Dalcin, V. Eijkhout, W. Gropp, D. Karpeyev, D. Kaushik, M. Knepley, L. Curfman McInnes, K. Rupp, B. Smith, S. Zampini, and H. Zhang, "PETSc User Manual", Argonne National Laboratory, Technical Report ANL-95/11 Rev 3.6 (2015).
26. M.A. Heroux and J.M. Willenbring, "Trilinos Users Guide", Sandia National Laboratories, Technical Report SAND2003-295 (2003).
27. R. Falgout, A. Cleary, J. Jones, E. Chow, V. Henson, C. Baldwin, P. Brown, P. Vassilevski and U. Meier Yang, "Hypre User's Manual", Lawrence Livermore National Laboratory (2015).
28. L.K.H. Leung, K.F. Rudzinski, B. Verma, D.C. Groeneveld and A. Vasic, "Thermalhydraulics Evaluation Package (TEP V3.0) – A User-friendly Software Package for Evaluating Thermalhydraulics Parameters in Tubes and Bundles", Proceedings of the 9th International Topical Meeting on Nuclear Reactor Thermalhydraulics (NURETH), San Francisco, USA (1999).
29. S.C. Yao, L.E. Hochreiter and W.J. Leech, "Heat-Transfer Augmentation in Rod Bundles Near Grid Spacers", *Journal of Heat Transfer*, 104 (1982) 76-81.
30. H.W. Hughes, "Implementation of Modified 37-Element Fuel Bundle at Darlington NGS – An Overview," *Proceedings of the 12th International Conference on CANDU Fuel*, Kingston, ON (2013).